Received: 7 October 2022 | Accepted: 22 November 2022

DOI: 10.1002/pamm.202200173

FFT-based simulation of evolving microstructures utilizing an adapting reduced set of Fourier modes

Christian Gierden[1,*], **Johanna Waimann**[1,2], **Bob Svendsen**[3,4], and **Stefanie Reese**[1]

[1] Institute of Applied Mechanics, RWTH Aachen University, Mies-van-der-Rohe-Straße 1, D-52074 Aachen, Germany

[2] Modeling and simulation techniques for systems of polycrystalline materials, RWTH Aachen University, Mies-van-der-Rohe-Straße 1, D-52074 Aachen, Germany

[3] Material Mechanics, RWTH Aachen University, Schinkelstraße 2, D-52062 Aachen, Germany

[4] Microstructure Physics and Alloy Design, Max-Planck-Institut für Eisenforschung GmbH, Max-Planck-Straße 1, D-40237 Düsseldorf, Germany

The mechanical behavior of a periodic heterogeneous microstructure may be predicted by using a fast Fourier transform (FFT) based simulation approach. To reduce the computational effort of this method, we introduced a model order reduction (MOR) technique utilizing a reduced set of Fourier modes for the computations in Fourier space. To increase the accuracy of this MOR technique we developed a geometrically adapted sampling pattern for choosing the considered Fourier modes based on the representation of phases within the microstructure. Since the phase distribution of, for example, martensite and austenite in a polycrystalline microstructure evolves with increasing mechanical or thermal loads, the set of considered Fourier modes should also evolve according to the underlying micromechanical fields. We present the accuracy and the adaptability of this adaptive reduced set of Fourier modes by investigating the micromechanical fields of a polycrystal considering such phase transformations.

1 Introduction

Investigating the mechanical behavior of periodic microstructures, the FFT-based simulation method [22,23] is an efficient and accurate alternative to classical FE-based simulations. This FFT-based microstructure simulation may also be used in terms of two-scale simulations resulting in a FE-FFT-based [13,28] approach, which also serves as an efficient and accurate alternative to the common FE^2 method. Nevertheless, considering complex macroscopic boundary value problems and highly resolved microstructures, both, the FE^2 and FE-FFT-based method are computationally expensive. To reduce the computational effort in this context, different strategies have been developed.

Concerning efficient two-scale simulation approaches utilizing the FE-FFT-based approach, different methods may be used: For example, using a coarse discretized microstructure for the two-scale simulation followed by a post-processing step for the generation of highly resolved microstructural results for macroscopic integration points of interest [5, 14] or using a database base instead of the FE-FFT-based approach, while this FE-FFT-based approach is only used in macroscopic critical areas [15]. A general overview on FE-FFT-based two-scale methods is given in [6].

Instead of utilizing such solution strategies, model order reduction (MOR) techniques for the FFT-based microstructure simulation have been introduced. These MOR techniques are for example based on a proper orthogonal decomposition (POD) [2], low-rank tensor approximations [30] or utilizing a reduced set of Fourier modes [12]. In this paper, we show how the concept of utilizing a reduced set of Fourier modes is used while accounting for evolving microstructures. A general overview on FFT-based methods for the simulation of periodic microstructures is given in [21, 27].

The FFT-based simulation using a reduced set of Fourier modes was introduced utilizing a fixed set of modes [4, 12]. In order to increase the accuracy of this MOR technique, a geometrically adapted selection of Fourier modes was developed in [8]. Since the geometry of a microstructure, such as the representation of phases within a microstructure, changes during different mechanical or thermal loading, an adaptively changing sampling pattern leads to even more accurate results throughout the simulation. In this context, a strain-based sampling pattern was introduced in [7], which adjusts the selection of Fourier modes to the strain field of the last load step. In the present paper, we show how this MOR technique performs investigating a polycrystalline microstructure incorporating solid-solid phase transformations between austenite and martensite.

The paper is structured as follows: In Section 2 the microstructural boundary value problem considering a polycrystalline microstructure with solid-solid phase transformations between austenite and martensite is briefly discussed. This is followed by introducing the reduced FFT-based microstructure simulation incorporating an adapting sampling pattern in Section 3. After discussing the numerical results in Section 4 the paper ends with a conclusion and outlook in Section 4.

* Corresponding author: e-mail christian.gierden@ifam.rwth-aachen.de, phone +49 241 80 25014, fax +49 241 80 22001

2 Microstructural boundary value problem and material model

Considering inhomogeneous microstructures, the quasi-static balance of linear momentum reads

$$\operatorname{div} \boldsymbol{\sigma}(\boldsymbol{x}) = \mathbf{0}\,, \tag{1}$$

while body forces on the microscale are neglected and small strain kinematics are assumed. The stress $\boldsymbol{\sigma}(\boldsymbol{x}) = \boldsymbol{\sigma}(\boldsymbol{x}, \boldsymbol{\varepsilon}(\boldsymbol{x}), \boldsymbol{\alpha}(\boldsymbol{x}))$ depends on the microscopic position $\boldsymbol{x}$, the total strain $\boldsymbol{\varepsilon}(\boldsymbol{x})$ and the internal variables $\boldsymbol{\alpha}(\boldsymbol{x})$. The total strain $\boldsymbol{\varepsilon}(\boldsymbol{x}) = \bar{\boldsymbol{\varepsilon}} + \tilde{\boldsymbol{\varepsilon}}(\boldsymbol{x})$ is additively split into a macroscopic part $\bar{\boldsymbol{\varepsilon}}$ and a microscopically fluctuating part $\tilde{\boldsymbol{\varepsilon}}(\boldsymbol{x})$. Finally, the overall macroscopic stress $\bar{\boldsymbol{\sigma}}$ and strain $\bar{\boldsymbol{\varepsilon}}$ fields are defined as volume averages of their local fields:

$$\bar{\boldsymbol{\sigma}} = \frac{1}{V}\int_\Omega \boldsymbol{\sigma}(\boldsymbol{x})\,\mathrm{d}\Omega \quad \text{and} \quad \bar{\boldsymbol{\varepsilon}} = \frac{1}{V}\int_\Omega \boldsymbol{\varepsilon}(\boldsymbol{x})\,\mathrm{d}\Omega\,. \tag{2}$$

To account for solid-solid phase transformations between austenite and martensite within a polycrystalline microstructure, we used a variational material model [9]. This model is extended to take into account irreversible phase transformations in [34] and to predict transformation induced plasticity in steel in [33]. The individual phases within this model are represented by their volume fractions λ_i, with $\lambda_0 = \lambda_A$ the volume fraction of austenite and $\lambda_{i>0} = \lambda_{M_i}$ the volume fractions of different martensitic variants. Each phase is characterized by an elastic stiffness tensor $\boldsymbol{C}_i$, a transformation strain $\boldsymbol{\eta}_i$ and a caloric part of the energy c_i. Taking into account the volume fractions of the individual phases, the corresponding effective quantities at one point j within the microstructure are given by:

$$\boldsymbol{\eta}^j_{\text{eff}} = \sum_{i=0}^{n} \lambda_i^j\, \boldsymbol{\eta}_i^j\,, \quad \boldsymbol{C}^j_{\text{eff}} = \left(\sum_{i=0}^{n} \lambda_i^j \left(\boldsymbol{C}_i^j\right)^{-1}\right)^{-1}, \quad c^j_{\text{eff}} = \sum_{i=0}^{n} \lambda_i^j\, c_i^j\,.$$

Using these effective quantities, the Helmholtz free energy Ψ^j within the point j in the microstructure is described as

$$\Psi^j = \frac{1}{2}\left(\boldsymbol{\varepsilon}^j - \boldsymbol{\eta}^j_{\text{eff}}\right) : \boldsymbol{C}^j_{\text{eff}} : \left(\boldsymbol{\varepsilon}^j - \boldsymbol{\eta}^j_{\text{eff}}\right) + c^j_{\text{eff}}\,, \tag{3}$$

while the effective stiffness tensor C^j_{eff} and transformation strains η^j_{eff} need to be rotated corresponding to the crystal structure within the polycrystal. Finally, the point-wise energy needs to be summed up, to compute the total energy $\Psi(\boldsymbol{\varepsilon}, \boldsymbol{\lambda})$.
To derive the material model, the principle of the minimum of dissipation potential is applied yielding

$$\mathcal{L} = \dot{\Psi}(\boldsymbol{\varepsilon}, \boldsymbol{\lambda}) + \mathcal{D}(\dot{\boldsymbol{\lambda}}) + cons \to \min_{\dot{\boldsymbol{\lambda}}}\,, \tag{4}$$

which is the minimization of a Lagrange function consisting of the rate of the Helmholtz free energy $\dot{\Psi}(\boldsymbol{\varepsilon}, \boldsymbol{\lambda})$, a dissipation function $\mathcal{D}(\dot{\boldsymbol{\lambda}})$ and constraints, in the examined case, the non-negativity of $\boldsymbol{\lambda}$ and the conservation of mass. The dissipation function $\mathcal{D} = r\,|\dot{\boldsymbol{\lambda}}|$ is given by the material dependent dissipation parameter r and the norm of the rate of the volume fractions $|\dot{\boldsymbol{\lambda}}|$. The minimization of Equation (4) leads to the evolution equation for the volume fraction of the individual phases

$$\dot{\lambda}_i^j = \beta^j \operatorname{dev}_{\mathcal{A}^j} P^j_{\mathrm{T}i} \quad \forall i \in \mathcal{A}^j \tag{5}$$

with the consistency parameter β^j and the active deviator $\operatorname{dev}_{\mathcal{A}^j} P^j_{\mathrm{T}i}$, which holds for the active set $\mathcal{A}^j = \left\{i|\lambda_i^j > 0\right\} \cup \left\{i|\lambda_i^j = 0 \wedge \dot{\lambda}_i^j > 0\right\}$. The active deviator is computed as

$$\operatorname{dev}_{\mathcal{A}^j} P^j_{\mathrm{T}i} = P^j_{\mathrm{T}i} - \frac{1}{n^j_{\mathcal{A}}} \sum_{k \in \mathcal{A}^j} P^j_{\mathrm{T}k} \tag{6}$$

with the thermodynamic driving force $P^j_{\mathrm{T}i}$ and the $n^j_{\mathcal{A}}$ active phases within $\mathcal{A}^j$. The thermodynamic driving force as well as the stress $\boldsymbol{\sigma}^j$ are defined as the partial derivatives of the energy (3) yielding

$$P^j_{\mathrm{T}i} = -\frac{\partial \Psi}{\partial \lambda_i^j} = \boldsymbol{\eta}^j : \boldsymbol{\sigma}^j + \frac{1}{2}\,\boldsymbol{\sigma}^j : \left(\boldsymbol{C}_i^j\right)^{-1} : \boldsymbol{\sigma}^j - c_i \tag{7}$$

$$\boldsymbol{\sigma}^j = \frac{\partial \Psi}{\partial \boldsymbol{\varepsilon}^j} = \boldsymbol{C}^j_{\text{eff}} : \left(\boldsymbol{\varepsilon}^j - \boldsymbol{\eta}^j_{\text{eff}}\right)\,. \tag{8}$$

Finally, the consistency parameter β^j is determined by the Karush-Kuhn-Tucker conditions

$$\Phi^j_{\mathrm{T}} = \operatorname{dev}_{\mathcal{A}^j} \boldsymbol{P}^j_{\mathrm{T}} \cdot \operatorname{dev}_{\mathcal{A}^j} \boldsymbol{P}^j_{\mathrm{T}} - r^2 \le 0\,, \quad \beta^j \ge 0\,, \quad \beta^j \Phi^j = 0\,. \tag{9}$$

These include the yield function Φ^j_T, which results from a Legendre transformation of the dissipation function $\mathcal{D}$.

3 Adaptively reduced FFT-based microstrucutre simulation

To solve the microscopic boundary value problem (BVP), the FFT-based fixed point solver [22, 23] is used incorporating a model order reduction technique based on a reduced set of Fourier modes. In order to use the spectral solver, the inhomogeneous BVP is transformed into an equivalent homogeneous BVP

$$\operatorname{div}\left[\boldsymbol{C}^0 : \boldsymbol{\varepsilon}(\boldsymbol{x})\right] + \operatorname{div}\boldsymbol{\tau}(\boldsymbol{x}) = \boldsymbol{0}\,, \tag{10}$$

by introducing the polarization stress $\boldsymbol{\tau}(\boldsymbol{x}) := \boldsymbol{\sigma}(\boldsymbol{x}) - \boldsymbol{C}^0 : \boldsymbol{\varepsilon}(\boldsymbol{x})$, which is the difference between the stress in the microstructure $\boldsymbol{\sigma}(\boldsymbol{x})$ and the stress in a homogeneous reference material $\boldsymbol{C}^0$ [10]. This equivalent homogeneous BVP may be solved using Green's function $\boldsymbol{G}^0(\boldsymbol{x}, \boldsymbol{x}')$ or Green's operator $\boldsymbol{\Gamma}^0(\boldsymbol{x}, \boldsymbol{x}')$ yielding the Lippmann-Schwinger equation [16]:

$$\boldsymbol{\varepsilon}(\boldsymbol{x}) = \bar{\boldsymbol{\varepsilon}} - \int_\Omega \boldsymbol{\Gamma}^0(\boldsymbol{x}, \boldsymbol{x}') : \boldsymbol{\tau}(\boldsymbol{x}')\,\mathrm{d}\boldsymbol{x}'\,. \tag{11}$$

In Fourier space this equation can directly be solved, since the occurring convolution integral ends up as simple multiplication

$$\hat{\boldsymbol{\varepsilon}}(\boldsymbol{\xi}) = \begin{cases} -\hat{\boldsymbol{\Gamma}}^0(\boldsymbol{\xi})\,\hat{\boldsymbol{\tau}}(\boldsymbol{\xi}) & \forall \quad \boldsymbol{\xi} \neq \boldsymbol{0} \\ \bar{\boldsymbol{\varepsilon}} & \forall \quad \boldsymbol{\xi} = \boldsymbol{0} \end{cases} \tag{12}$$

and Green's function $G^0_{ik}(\boldsymbol{\xi}) = (C^0_{ijkl}\,\xi_j\,\xi_l)^{-1}$ and Green's operator $\hat{\Gamma}^0_{ijkl}(\boldsymbol{\xi}) = \frac{1}{2}\left(\hat{G}^0_{ik}(\boldsymbol{\xi})\,\xi_j\,\xi_l + \hat{G}^0_{jk}(\boldsymbol{\xi})\,\xi_i\,\xi_l\right)$ are explicitly known and just depending on the homogeneous reference material behavior and the wave vector $\boldsymbol{\xi}$, that gathers all the Fourier modes considered within the simulation.
Moulinec and Suquet introduced a fixed point scheme computing the polarization stress in real space, which is then transferred into Fourier space and used to solve the Lippmann-Schwinger equation (12) in Fourier space to compute the strain for the next iteration [22, 23]. Considering polycrystalline microstructures, this FFT-based microstructure simulation was first used in [17, 18].

In order to reduce the computational effort of this spectral solver, a model order reduction technique utilizing just a reduced set of Fourier modes for solving the Lippmann-Schwinger equation in Fourier space was introduced in [12]. To increase the accuracy of this technique, we introduced a geometrically adapted sampling pattern [8]. This technique is based on a given and fixed representation of phases within the microstructure. Since the phases within a microstructure, for example in a polycrystal, may not be clearly defined and even evolve, we presented a strain-based sampling pattern in [7]. The idea of the strain-based sampling pattern is to consider the norm of the converged strain field of a given load step $||\boldsymbol{\varepsilon}^i(\boldsymbol{x})||$ for the definition of the reduced set of Fourier modes. This strain field is transferred into Fourier space and the sampling pattern for the next load step $\mathcal{S}^{i+1}_\varepsilon$ is defined by a given percentage $\mathcal{R}$ of Fourier modes with the highest amplitudes needed to capture the norm of the strain field in Fourier space:

$$\mathcal{S}^{i+1}_\varepsilon : \text{ Fourier modes with the highest amplitudes of } \mathcal{FFT}\left\{||\boldsymbol{\varepsilon}^i(\boldsymbol{x})||\right\}$$

This techniques leads to an evolving sampling pattern that is always adapting to the strain within a microstructure and therefore to changes, such as solid-solid phase transformations between austenite and martensite, as can be seen in Section 4.

4 Numerical results

To show the adaptability and accuracy of the strain-based sampling pattern for evolving microstructures, we considered a polycrystalline nickel titanium (NiTi) alloy (known for the shape memory effect) incorporating phase transformations between austenite and twelve different martensitic variants. Fig. 1 shows the polycrystalline microstructure, i.e. the orientation of the first Euler angle φ, and the lattice structure of the austenite and martensite.

The following material parameters are considered for the simulation: The dissipation parameter is set to $r = 0.006\,\mathrm{GPa}$, the caloric energies read $c_A = -0.03\,\mathrm{GPa}$ and $c_{M_i} = 0.0\,\mathrm{GPa}$ and the stiffness tensors and transformation strains of the individual phases are taken from [11, 31]. For the simulations, we used a fine discretization with 255×255 grid points, while only $\mathcal{R} = 1\%$ of Fourier modes were utilized for the computations in Fourier space. Fig. 2 shows the overall macroscopic and microstructural results and their differences from the reference solution computed with the full set of Fourier modes. Also shown is the stepwise changing sampling pattern for loading and unloading of the microstructure by $\bar{\varepsilon}_{xx} = 0.04$.

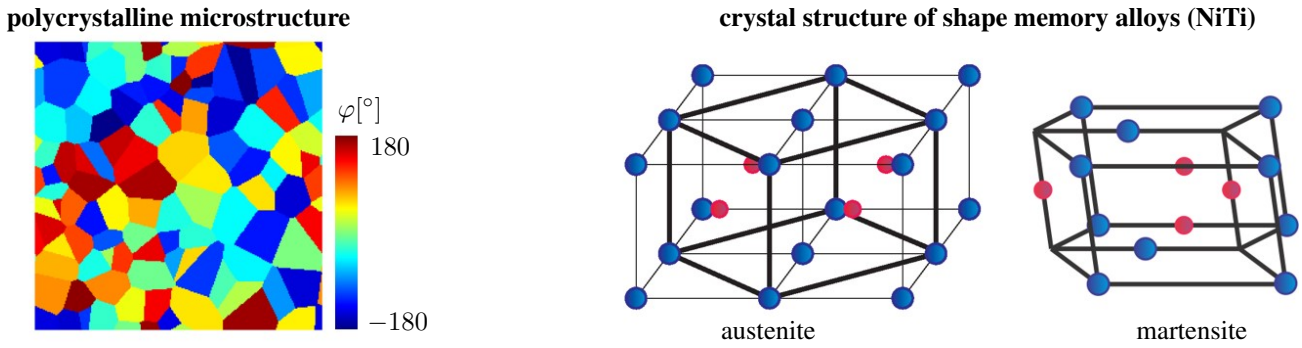

Fig. 1: Left: Orientation of the first Euler angle φ of the polycrystal. Right: Crystal structure of austenite and martensite [25].

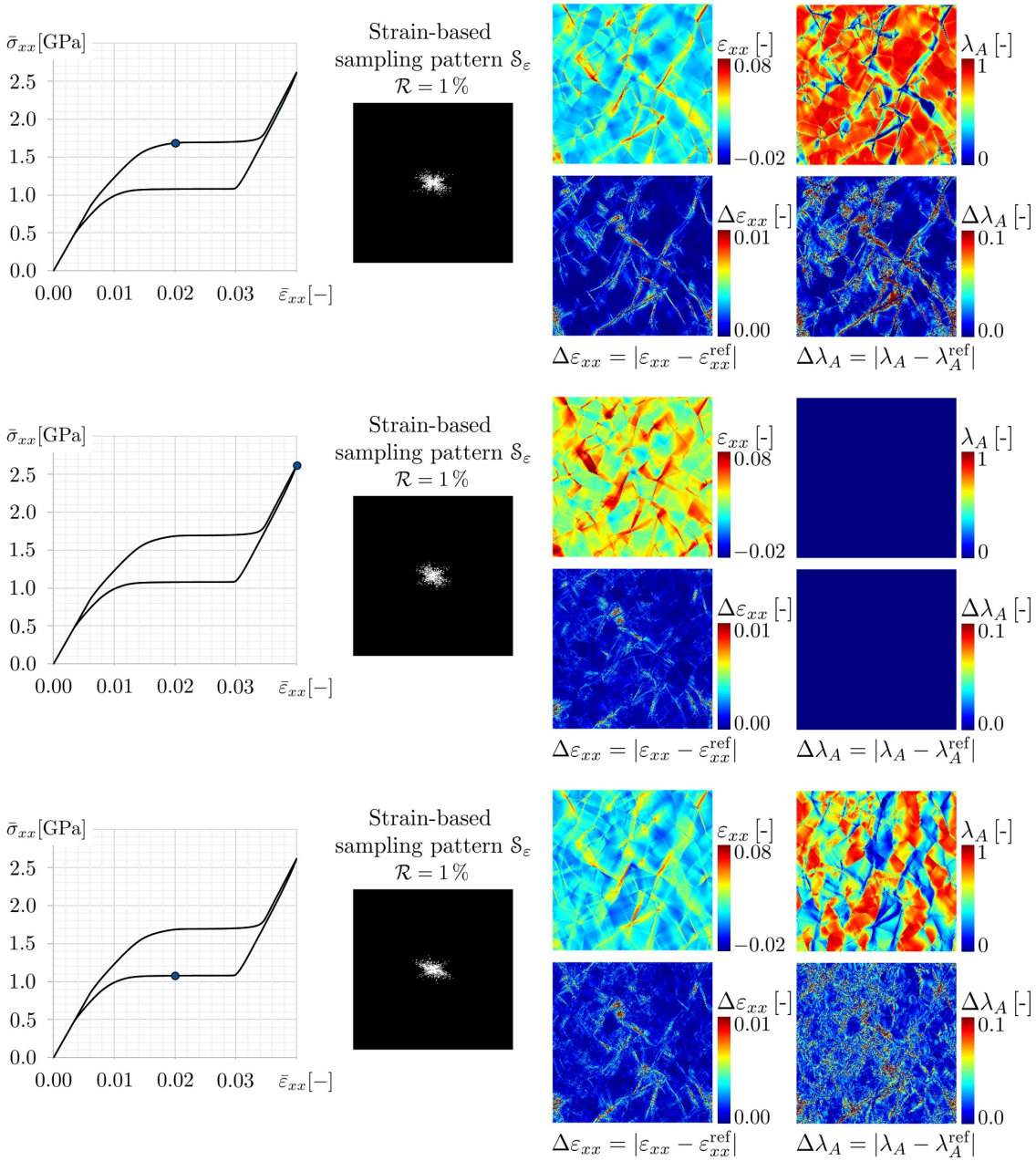

Fig. 2: Overall stress-strain diagram, sampling pattern, microscopic strain ε_{xx} and volume fraction of the austenite λ_A and their differences compared to the reference solution for three different load steps of the loading/unloading paths.

The overall macroscopic stress-strain diagram shows the typical hysteresis curve for the pseudoelastic material behavior of a shape memory alloy. Starting with a pure austenitic microstructure and linear elastic material behavior, occurring phase

transformations from austenite to martensite at certain points in the microstructure continuously lead to a plateau within the macroscopic stress-strain curve. After the transformation of the entire microstructure is completed, again a linear elastic material behavior, related to the material behavior of a pure martensitic microstructure, is observed. When the microstructure is unloaded, the same behavior occurs, but with a lower stress plateau, which refers to the back transformation from martensite to austenite.

Regarding the macroscopic material behavior, the total error associated with the model order reduction is extremely small. Therefore, the curves of the reduced and the unreduced solution overlap, and in Fig. 2 on the left-hand side, only one macroscopic stress-strain curve can be seen.

Concerning the microstructural fields, in Fig. 2 on the right side the strain ε_{xx} and the volume fraction of austenite λ_A as well as the corresponding absolute differences compared to the reference solution computed with the full set of Fourier modes are shown for three specific load steps. It can be seen, that the differences are the highest while phase transformations take place within the microstructure. Before and after the occurrence of these phase transformations, the error related to the volume fraction of austenite is zero, since a pure martensitic or austenitic microstructure is present without inhomogeneities related to the phase mixture of the microstructure. Accordingly, the error with respect to the microscopic strain field ε_{xx} is also lower when the phase transformations are completed.

In addition, the strain-based sampling pattern with 1% of Fourier modes for the three different load steps is shown as well. Since this sampling pattern is always adapted to the strain field of the last load step, it changes from load step to load step, whenever a nonlinear material behavior is present.

Although the results shown in Fig. 2 are obtained by considering only 1% of Fourier modes for the computations in Fourier space, the maximum relative macroscopic and microscopic errors related to the stress fields that occur during the entire simulation (loading and unloading path) are as follows:

$$\bar{\mathcal{E}}_\sigma = \frac{||\bar{\boldsymbol{\sigma}} - \bar{\boldsymbol{\sigma}}^{\mathrm{ref}}||}{||\bar{\boldsymbol{\sigma}}^{\mathrm{ref}}||} \leq 0.04\% \quad \text{and} \quad \mathcal{E}_\sigma = \frac{1}{n}\sum_n \frac{||\boldsymbol{\sigma}(n) - \boldsymbol{\sigma}(n)^{\mathrm{ref}}||}{||\boldsymbol{\sigma}(n)^{\mathrm{ref}}||} \leq 0.25\% \,.$$

The accuracy and the reduction of the CPU time are influenced in an opposing way by the considered number of Fourier modes. The lower the number of used Fourier modes, the lower is the CPU time, but the higher is the error. In the present case, the reduction to 1% of Fourier modes leads to the aforementioned accuracy, while a CPU time reduction of up to 20% is achieved.

5 Conclusion and outlook

We presented the application of the reduced FFT-based microstructure simulation with an adapting set of Fourier modes to an evolving microstructure with solid-solid phase transformations between austenite and martensite. Specifically, we investigated a nickel-titanium alloy (NiTi) known for its shape memory effect. Doing that and considering only 1% of Fourier modes, a CPU time reduction of up to $20\,\%$ can be achieved compared to calculations using the full set of Fourier modes. At the same time, the total macroscopic and microscopic errors related to the stress fields are below $\bar{\mathcal{E}}_\sigma \leq 0.04\,\%$ and $\mathcal{E}_\sigma \leq 0.25\,\%$, respectively, throughout the entire loading and unloading paths while the highest errors occur during the process of phase transformations.

Future works will address and further investigate various aspects of improving the FFT-based microstructure simulation with a reduced set of Fourier modes. In this context, interesting topics are related to decreasing the computational effort of the stress evaluations (e.g. by using a clustered microstructure [20, 36] for the stress evaluations in real space [32]), using more efficient solvers (e.g. Nesterov's fast gradient method [26] or the Heavy ball method [1]), or reducing the effect of Gibbs oscillations [3] on the convergence behavior (e.g. by using second [19,24] or higher order [29] finite difference approximations of the Lippmann-Schwinger operator or the rotated scheme of Willot [35]).

Acknowledgements The work is funded by the Deutsche Forschungsgemeinschaft (DFG, German Research Foundation) – Projektnummer 223500200 – TRR 136. We gratefully acknowledge the financial support of the subproject M03. Open access funding enabled and organized by Projekt DEAL.

References

[1] F. Ernesti, M. Schneider, and T. Böhlke, Comput. Methods Appl. Mech. Eng. **363**, 112793 (2020).
[2] C. Garcia-Cardona, R. Lebensohn, and M. Anghel, Int. J. Numer. Methods Eng. **112(6)**, 578-600 (2017).
[3] J.W. Gibbs, Nature **59**, 200-200 (1898).
[4] C. Gierden, J. Kochmann, K. Manjunatha, J. Waimann, S. Wulfinghoff, B. Svendsen, and S. Reese, Proc. Appl. Math. Mech. **19**, e20190003 (2019).
[5] C. Gierden, J. Kochmann, J. Waimann, T. Kinner-Becker, J. Sölter, B. Svendsen, and S. Reese, Comput. Methods in Appl. Mech. Eng. **374**, 113566 (2021).

[6] C. Gierden, J. Kochmann, J. Waimann, B. Svendsen, and S. Reese, Arch. Comput. Methods Eng. **29**, 4115-4135 (2022).
[7] C. Gierden, J. Waimann, B. Svendsen, and S. Reese, Comput. Methods Mater. Sci. **21 (1)**, 51-58 (2021).
[8] C. Gierden, J. Waimann, B. Svendsen, and S. Reese, Comput. Methods in Appl. Mech. Eng. **386**, 114131 (2022).
[9] K. Hackl and R. Heinen, Continuum Mech. Thermodyn. **19 (8)**, 499–510 (2008).
[10] Z. Hashin and S. Shtrikman, J. Mech. Phys. Solids **10 (4)**, 335-342 (1962).
[11] P. Junker, Inst. Mech. Schriftenreihe (2011).
[12] J. Kochmann, K. Manjunatha, C. Gierden, S. Wulfinghoff, B. Svendsen, and S. Reese, Comput. Methods in Appl. Mech. Eng. **347**, 622-638 (2019).
[13] J. Kochmann, S. Wulfinghoff, S. Reese, J. R. Mianroodi, and B. Svendsen, Comput. Methods in Appl. Mech. Eng. **305**, 89-110 (2016).
[14] J. Kochmann, S. Wulfinghoff, S. Reese, B. Svendsen, L. Ehle, and J. Mayer, Comput. Mech. **61(6)**, 751-764 (2018).
[15] J. Köbler, N. Magino, H. Andrä, F. Welschinger, R. Müller and M. Schneider, Comput. Methods Appl. Mech. Eng. **373**, 113522 (2021).
[16] E. Kröner, Arch. Ration. Mech. Anal. **4(1)**, 273–334 (1959).
[17] R.A. Lebensohn, Acta Mater. **49 (14)**, 2723-2737 (2001).
[18] R.A. Lebensohn, A.K. Kanjarla and R. Eisenlohr, Int. J. Plast. **32**, 59-69 (2012).
[19] R.A. Lebensohn and A. Needleman, J. Mech. Phys. Solids **97**, 333-351 (2016).
[20] Z. Liu, M.A. Bessa and W.K. Liu, Comput. Methods in Appl. Mech. Eng. **306**, 319-341 (2016).
[21] S. Lucarini, M.V. Upadhyay and J. Segurado, Model. Simul. Mater. Sci. Eng. **30**, 023002 (2021).
[22] H. Moulinec and P. Suquet, C. R. Acad. Sci., Série II **318 (11)**, 1417-1423 (1994).
[23] H. Moulinec and P. Suquet, Comput. Methods in Appl. Mech. Eng. **157(1-2)**, 69-94 (1998).
[24] W.H. Müller, IUTAM Symposium on Transformation Problems in Composite and Active Materials , 61-72 (1998).
[25] K. Otsuka and X. Ren, Prog. Mater. Sci. **50(5)**, 511-678 (2005).
[26] M. Schneider, Comput. Methods Appl. Mech. Eng. **315**, 846-866 (2017).
[27] M. Schneider, Acta Mech. **232**, 2051–2100 (2021).
[28] J. Spahn, H. Andrä, M. Kabel, and R. Müller, Comput. Methods in Appl. Mech. Eng. **268**, 871-883 (2014).
[29] A. Vidyasagar, W.L. Tan, and D.M. Kochmann, J. Mech. Phys. Solids **106**, 133-151 (2017).
[30] J. Vondřejc, D. Liu, M. Ladecký and H.G. Matthies, Comput. Methods in Appl. Mech. Eng. **364**, 112890 (2020).
[31] M. F.-X. Wagner and W. Windl, Acta Mater. **56(20)**, 6232–6245 (2008).
[32] J. Waimann, C. Gierden, A. Schmidt, B. Svendsen and S. Reese, Key Eng. Mater. **926**, 2285-2292 (2022).
[33] J. Waimann, P. Junker and K. Hackl, J Mech Behav Mater **24 (5-6)**, 153-159 (2015).
[34] J. Waimann, P. Junker and K. Hackl, Shape Mem. Superelasticity **3 (2)**, 124-138 (2017).
[35] F. Willot, CR Mécanique **343 (3)**, 232-245 (2015).
[36] S. Wulfinghoff, F. Cavaliere and S. Reese, Comput. Methods in Appl. Mech. Eng. **330**, 149-179 (2018).